Peer Reviewed Paper openaccess

Can hyperspectral imaging be used to map corrosion products on outdoor bronze sculptures?

Emilio Catelli,[a,*] Lise Lyngsnes Randeberg,[b,*] Helena Strandberg,[c] Bjørn Kåre Alsberg,[d,†] Assimo Maris[e] and Lily Vikki[f]

[a]Department of Chemistry, Norwegian University of Science and Technology (NTNU), N-7491 Trondheim, Norway. E-mail: e.catelli2@gmail.com ORCID: https://orcid.org/0000-0002-9634-1381

[b]Department of Electronic Systems, Norwegian University of Science and Technology (NTNU), N-7491 Trondheim, Norway. E-mail: lise.randeberg@ntnu.no. ORCID: https://orcid.org/0000-0003-2608-3759

[c]Helena Strandberg Konservator AB, 414 53, Göteborg, Sweden. ORCID: https://orcid.org/0000-0001-6898-5529

[d]Department of Chemistry, Norwegian University of Science and Technology (NTNU), N-7491 Trondheim, Norway.

[e]Department of Chemistry "G. Ciamician", Alma Mater Studiorum, University of Bologna, 40100 Bologna, Italy. ORCID: https://orcid.org/0000-0003-2644-0023

[f]Oslo kommunes kunstsamling/City of Oslo Art Collection, Kulturetaten/Agency for Cultural Affairs, 0184 Oslo, Norway

The application of hyperspectral imaging in the field of cultural heritage investigation is growing rapidly. In this study, short wavelength infrared hyperspectral imaging (960–2500 nm) has been explored as a potential non-invasive technique for *in situ* mapping of corrosion products on bronze sculptures. Two corrosion products, brochantite and antlerite, commonly found on the surfaces of outdoor bronze monuments, were considered. Their spatial distribution was investigated on the surface of the bronze sculpture *The Man with the Key* by Auguste Rodin in Oslo. The results demonstrate that hyperspectral imaging combined with image analysis algorithms can display the distribution of the two corrosion products in different areas (unsheltered and partially sheltered) of the sculpture.

Keywords: hyperspectral imaging, outdoor bronze sculpture, image analysis, bronze corrosion

Introduction

Hyperspectral imaging (HSI) is a non-invasive technique that combines imaging and spectroscopy.[1] Spatial and spectral information is thus obtained simultaneously and can be used to visualise the spatial distribution of characteristic chemical properties on surfaces. HSI was initially developed for remote sensing but it has also found various applications in medicine,[2] forensic investigations[3] and food analysis.[4] As HSI can be applied *in situ*, this method is suited for investigating fine art objects that cannot be moved from their display location.[1] HSI has therefore been used to study paintings,[5] delicate and fragile manuscripts[6] and even art objects created from

[†]Passed away 27 December 2017

Correspondence
Emilio Catelli (e.catelli2@gmail.com)
Lise Lyngsnes Randeberg (lise.randeberg@ntnu.no)

Received: 6 March 2018
Revised: 10 September 2018
Accepted: 12 September 2018
Publication: 8 October 2018
doi: 10.1255/jsi.2018.a10
ISSN: 2040-4565

Citation
Emilio Catelli *et al.*, "Can hyperspectral imaging be used to map corrosion products on outdoor bronze sculptures?", *J. Spectral Imaging* **7,** a10 (2018). https://doi.org/10.1255/jsi.2018.a10

plastic.[7] These investigations aim at mapping inorganic or organic constituents on the art objects to obtain information on their materials and state of conservation. An expanded application of this technology to other types of heritage objects would most likely be beneficial.

Following this line of thought and keeping in mind that the HSI equipment is robust and can be operated *in situ*, this work attempted to use this technique to investigate atmospheric corrosion of outdoor bronze artefacts exposed to urban environments. It is known that, in the presence of sulfur oxides and acid rain which are common in urban areas, two basic copper (II) sulfates, brochantite [$Cu_4SO_4(OH)_6$], and antlerite [$Cu_3SO_4(OH)_4$], form as the most common basic copper (II) sulfate corrosion products on outdoor bronze sculptures.[8] The two compounds are green and form as a result of complex electrochemical processes.[9,10] Antlerite was found to be stable in more acidic condition than brochantite.[9,11]

The detection of these products allows assessment of the general condition of sculptures and the planning of their protection intervention. Laboratory analysis of microsamples collected from discrete spots provides detailed characterisation of these corrosion products, but does not give their spatial distribution over large areas. HSI, on the other hand, may provide additional spatial distribution in a non-invasive manner at high resolution. This is important since antlerite crusts are more soluble and less protective than brochantite[12] and the areas in which antlerite is located are thus more prone to erosion by rainwater.[11] In addition, different corrosion mechanisms may operate on the same monument according to the particular micro-environmental conditions established on limited areas.[13] Therefore, the spatial distribution of corrosion products can be crucial in bronze sculpture investigation, especially since corroboration with the macro-environmental conditions does not always allow the composition of the corrosion products to be inferred in a straightforward way.

In this study, a short wavelength infrared (SWIR) HSI instrument (960–2500 nm) was operated *in situ* to investigate the spatial distribution of brochantite and antlerite on the surface of an outdoor bronze sculpture. Prior to the *in situ* investigation of the sculpture, reference reflectance spectra of synthetic brochantite and antlerite were collected in the laboratory by means of the same instrument to create a reference dataset. The hyperspectral device employed here was chosen because the two corrosion products showed distinct spectral features in the SWIR region.[14,15]

The sculpture investigated is *The Man with the Key*. It represents Jean d'Aire and it is the first individual figure cast in bronze from the famous group *Les Bourgeois de Calais* (*The Burghers of Calais*) by Auguste Rodin.[16] The sculpture was cast by Jacques Petermann in Brussels (Belgium)[16] and the bronze composition (in %wt), determined on an unpatinated area by X-ray fluorescence (XRF) spectrometry is approximately Cu 90, Sn 4 and Zn 6, with traces of Pb, Ti and Fe. Since 1902 it has resided at "Solli plass", a traffic-congested area in the city centre of Oslo (Norway). This place was likely subjected to high levels of SO_2 pollution and acidic rain conditions. The sculpture is in a state of advanced degradation and was relocated to the Vigeland Museum's courtyard for conservation. The HSI investigation was performed there.

Experimental section

Data acquisition and pre-processing

Hyperspectral images were collected with a HySpex SWIR-320 hyperspectral camera from Norsk Elektro Optikk AS (Norway) using the push broom scanning method. The camera covers the SWIR range 960–2500 nm with a spectral resolution of 5.7 nm for a total of 256 wavelengths. In this study, the first three wavelengths were discarded due to the presence of artefacts in the spectra.

The hyperspectral images were organised as a three-dimensional cube (datacube) with two spatial dimensions, pixels (x,y), and one wavelength dimension (λ). Data were pre-processed using Matlab (the Mathworks Inc., USA) programs.

Brochantite and antlerite corrosion products were synthesised according to the method in Reference 17 and characterised by X-ray diffraction (Figure SM1 in the Supplementary Material). Afterwards, they were scanned in the laboratory by means of the SWIR-320 camera. Primary data were radiometrically calibrated and successively converted into reflectance using a Spectralon reflectance standard (SRT-50-050 reflectance target, 12.7 × 12.7 cm, ACAL, BFi Nordic AB, Uppsala, Sweden). The resulting images were processed with the Minimum Noise Fraction (MNF) algorithm[18] to minimise noise. Reference spectra of the two corrosion products were extracted manually from the corrected datacube.

In situ analyses of the sculpture were performed under a party tent, which partly protected it from natural illumination. The hyperspectral camera was placed on a motorised translation stand with a working distance of approximately 30 cm. Areas of approximately 10 × 7 cm were scanned under natural (low) and artificial illumination (dominant). After radiometric calibration, conversion into reflectance was obtained by using a hyperspectral image of the above-mentioned Spectralon reflectance target, collected in the laboratory under similar artificial illumination conditions as used *in situ* for the sculpture. No correction for uneven illumination distribution was applied to the images. The Spectralon data were collected in the laboratory to reduce the contribution of water vapour in the spectra, which was high during the outdoor measurements (which took place on a rainy day). The reduction of water vapour in the white reference spectra helped to prevent issues of non-efficient subtraction of water vapour signals in the reflectance-corrected data. The spectra profile of the Spectralon white reference overlapped well with those of a white reference material scanned *in situ*, supporting the use of the Spectralon data collected in the laboratory for reflectance correction.

The HS images from the sculpture were pre-processed by averaging 2 × 2 pixels to remove noise, and successively cropped to select the interesting area. The resulting HS images collected from an unsheltered and partially sheltered area have 160 × 103 and 160 × 145 pixels, respectively.

In situ XRF spectrometry was performed by a portable Thermo Nicolet Niton XI3t 900 instrument operated in the "General Metals" mode in the range 0–51 keV. Absorption mid-infrared spectra were recorded in KBr tablets (potassium bromide FT-IR grade ≥ 99 %, Sigma Aldrich Inc.) by means of a Thermo Nicolet NEXUS FT-IR instrument. The spectra were acquired in the range (4000–400 cm^{-1}) by averaging 64 scans for the signal and the background, with a spectral resolution of 4 cm^{-1}. X-ray diffraction data were collected using a Bruker D8-davinci instrument equipped with a V6 slit. The scanned interval was from 10° to 60° (2θ) stepping at 0.013°. Diffraction patterns were interpreted by the PDF (ICDD) built-in library of standard compounds.

Hyperspectral data analysis

Hyperspectral data analysis was performed by in-house Matlab algorithms. Initially, data were explored by the singular value decomposition (SVD) method followed by Iterative Key Set Factor Analysis (IKSFA)[19,20] algorithms. Further, the spatial distribution of the corrosion products was obtained using the Spectral Angle Mapper (SAM) algorithm.[21] This approach to HSI data analysis has been previously used for investigating the spatial distribution of inorganic pigments in manuscript illuminations.[22] In detail, the pre-processed datacube was, first, converted into a two-dimensional matrix by a procedure called "unfolding", where pixels are the objects (rows) and wavelengths are the variables (columns). Second, SVD was applied to achieve the factorisation of the above matrix. By inspecting the eigenvalues thus obtained, one can infer the number of significant factors (*n*) that best characterise the data. Third, IKSFA was performed on the "unfolded" matrix to extract the best key set of raw spectra defined by the *n* selected significant factors. Each selected raw spectrum thus obtained may be somewhat different from that of a pure compound, as interference from noise or other signals (i.e. water vapour, bands from other compounds) may affect it. However, it is as close to a pure compound spectrum as possible. Since each IKSFA spectrum is dominated by a particular pure spectrum, its absorption bands will be used for identification of the pertinent corrosion product. Finally, the SAM algorithm was applied to obtain the spatial distribution of the identified corrosion products. SAM assesses the degree of similarity (by an angle expressed in radians) of spectra in the datacube with a selected reference spectrum. In this study, the reference spectrum is the laboratory-recorded spectrum of the pure corrosion product. The output from the SAM-algorithm is displayed as a greyscale image where black indicates the highest similarity with each reference spectrum, and white, the lowest.

Spectral bands assignment

The infrared-active fundamental vibrations of brochantite and antlerite have been studied by Secco[23] and occur just outside the SWIR range, at lower wavelengths. Therefore, the vibrational processes that produce features observed in the SWIR spectrum are overtones and combination bands of the fundamentals, and are mainly related to the OH group motions.[24,25]

In order to assign the most prominent features of brochantite and antlerite in the SWIR range, the following procedure was devised: initially, the fundamental stretching (ν) and bending (δ) OH vibrational wavenumbers of brochantite and antlerite reported by Secco[23] in the mid-infrared region (2500–25,000 nm or 4000-

400 cm^{-1}) were selected. It is worth noting that both molecules present several OH-type bands corresponding to a different degree of hydrogen bonding in the crystal. Successively, for each compound, the spectral range where the first OH overtone band lies was estimated by doubling the wavenumbers of the OH stretching vibrations. The limits of the range were settled by considering the lowest and highest values obtained from the above calculation. The combination bands range was determined by summing stretching and bending wavenumbers related to the same OH-type. Following a conversion to wavelengths, the spectral range of combination bands (ν + δ) for brochantite was identified between 2285 nm and 2371 nm while, for antlerite, the range was 2275–2310 nm. Conversely, the first overtone range was between 1390 nm and 1528 nm for brochantite and 1397–1433 nm for antlerite. Finally, band assignment was performed by comparing the calculated overtone or combination ranges with the position of the spectral bands of each pertinent compound. For a more detailed overview concerning band assignment, the reader is referred to the spectroscopic studies of brochantite and antlerite undertaken by K.M. Reddy[14] and R. Rama Subba Reddy.[15]

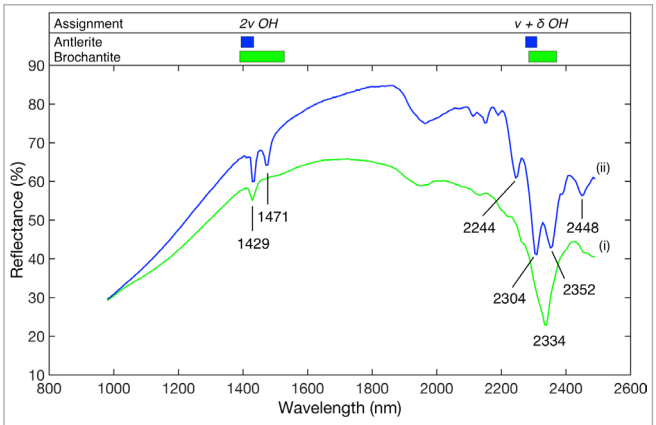

Figure 1. Reference spectra recorded in laboratory of (i) brochantite and (ii) antlerite from a SWIR hyperspectral camera. Upper part: spectral regions (wavelength scale) of first overtone and combination bands of OH motions calculated for the two compounds from the experimental fundamentals, assuming a harmonic potential.

Results and discussion

The reflectance spectra of standard brochantite and antlerite specimens in the SWIR region are presented in Figure 1. As it is possible to observe, the two compounds can be clearly distinguished based on their different spectral profiles. The upper part of Figure 1 shows the calculated ranges of overtones and combination bands for the two compounds, which were used for band assignment. Among the most prominent spectral features, brochantite shows a strong broad band at 2334 nm, which lies in the combination band range calculated for this compound (Figure 1). For this reason, the band can be assigned to the combination of OH stretching and OH bending modes. Following this, the weak, isolated, band at 1429 nm is assigned to the first νOH overtone. This assignment is also in accordance with the publication of Reddy.[14] Antlerite, on the other hand, shows a pattern of four strong bands in the 2500–2200 nm range, positioned at 2448, 2352, 2304 and 2244 nm, respectively, and two isolated weak bands at 1429 and 1471 nm. The band at 2304 nm has been assigned to the combination νOH + δOH while the band located at approximately 1429 nm has been ascribed to the first overtone of νOH fundamentals.[15] The main spectral features of the two compounds discussed above are in good agreement with those reported in the literature.[26]

The HSI examination of the sculpture focused on two areas. The first [Figure 2c (1), left shoulder] is unsheltered, while the second [Figure 2d (2), near the right leg] is partially sheltered. According to their orientation, each of the above areas may be subjected to different microenvironmental conditions. The results for the unsheltered area are presented in Figure 3 along with an image of the investigated sculpture and the instrumentation. An RGB picture of the unsheltered area (Figure 3b) shows an almost uniform yellowish-green surface. SVD demonstrates that one single major factor accounts for the observed spectral features. By means of IKSFA, the raw spectrum was extracted [Figure 3c(i)] and assigned to brochantite due to the characteristic combination band νOH + δOH at 2334 nm. The additional bands in the ranges 1300–1400 nm and 1800–1900 nm stem most likely from water vapour in the atmosphere. The SAM image (Figure 3d), obtained using the standard spectrum of brochantite [Figure 1(i)] as reference spectrum reveals the presence of brochantite in all the green areas. The dark spots in Figure 3b appear as white in Figure 3d, meaning low similarity with the spectrum of brochantite. The spectral behaviour of these spots is represented by the second spectrum extracted by IKSFA and shown in Figure 3c (ii). However, this spectrum shows a low signal-

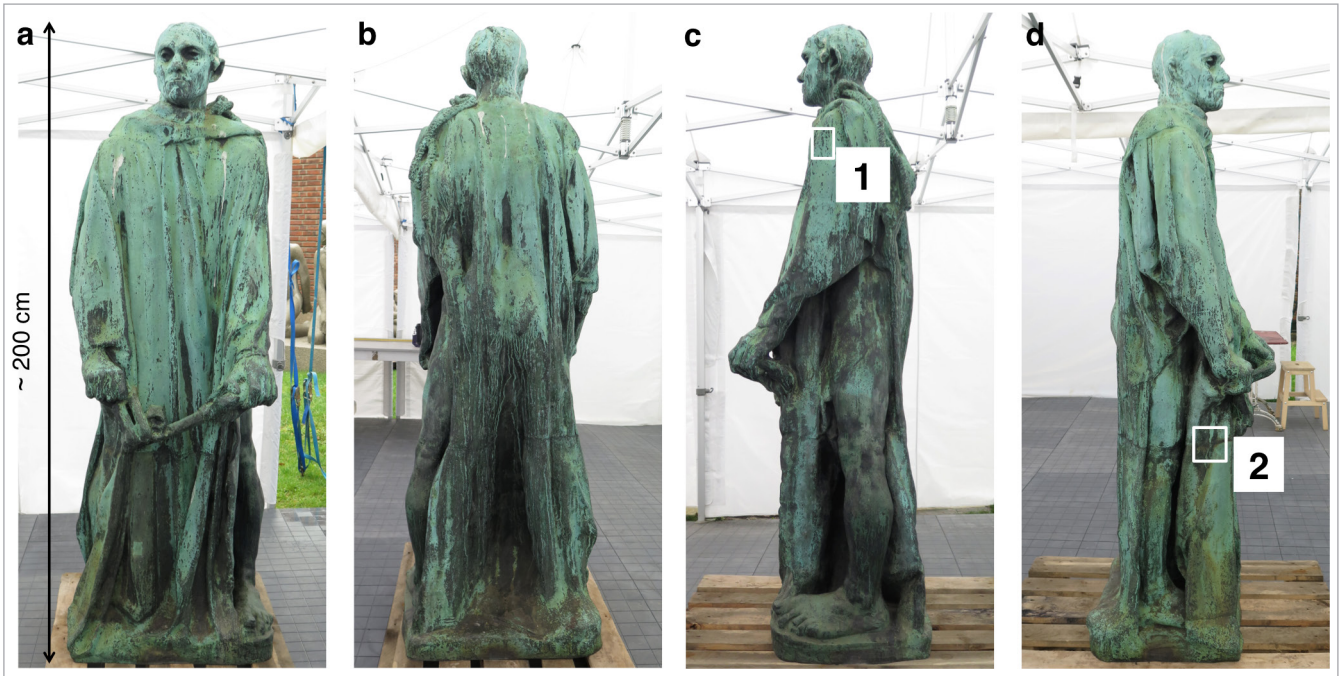

Figure 2. The sculpture *The Man with the Key* by Auguste Rodin—photo by Helena Strandberg; (a) front view; (b) back view; (c) left side view with 1) unsheltered investigated area; (d) right-side view with 2) partially sheltered investigated area.

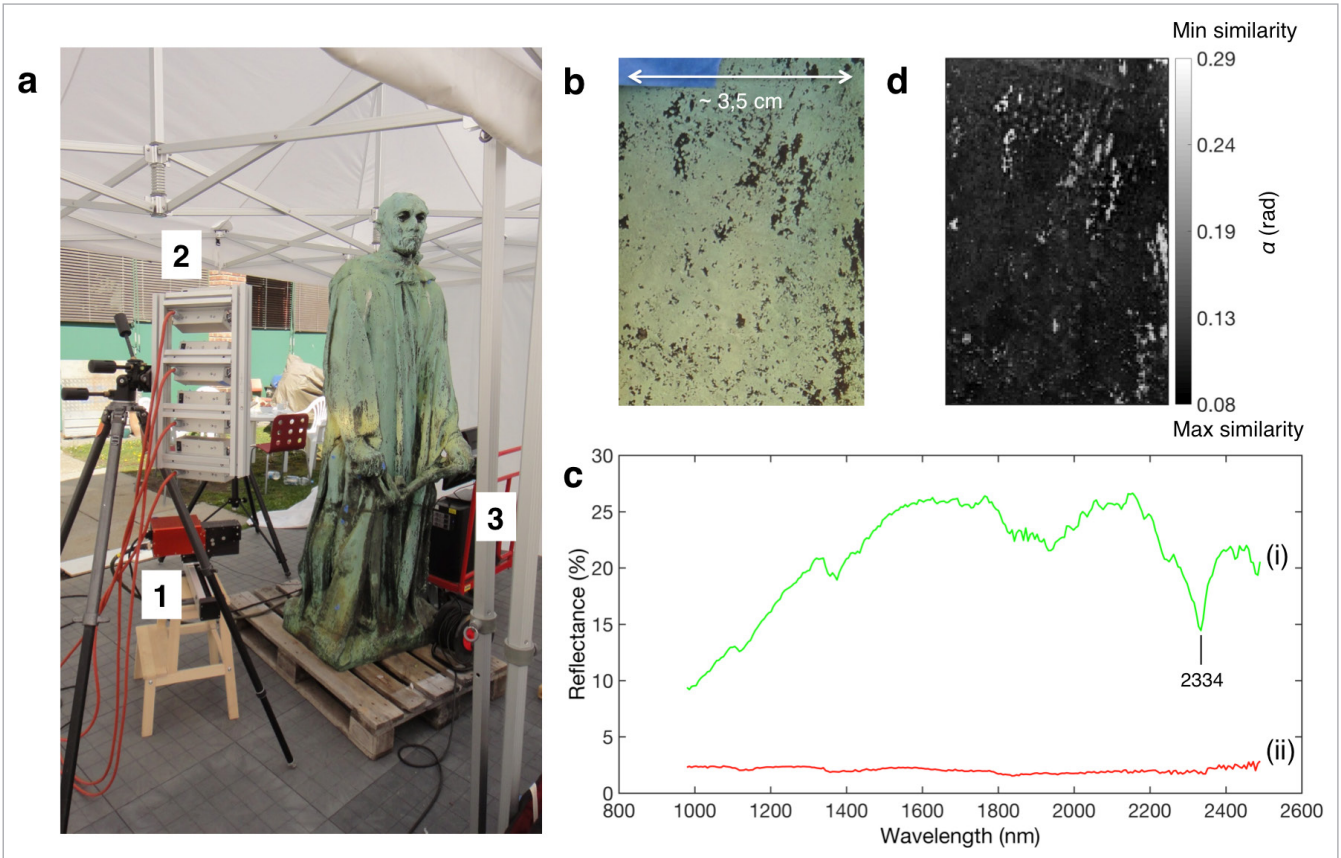

Figure 3. Experimental setup and results for the unsheltered area. (a) The examined sculpture and the equipment 1) SWIR hyperspectral camera; 2) light sources; 3) computer for data acquisition; (b) RGB image of the unsheltered investigated area; (c) spectra extracted by IKSFA where spectrum (i) is assigned to brochantite and (ii) is an unassigned spectrum; (d) SAM image of brochantite distribution.

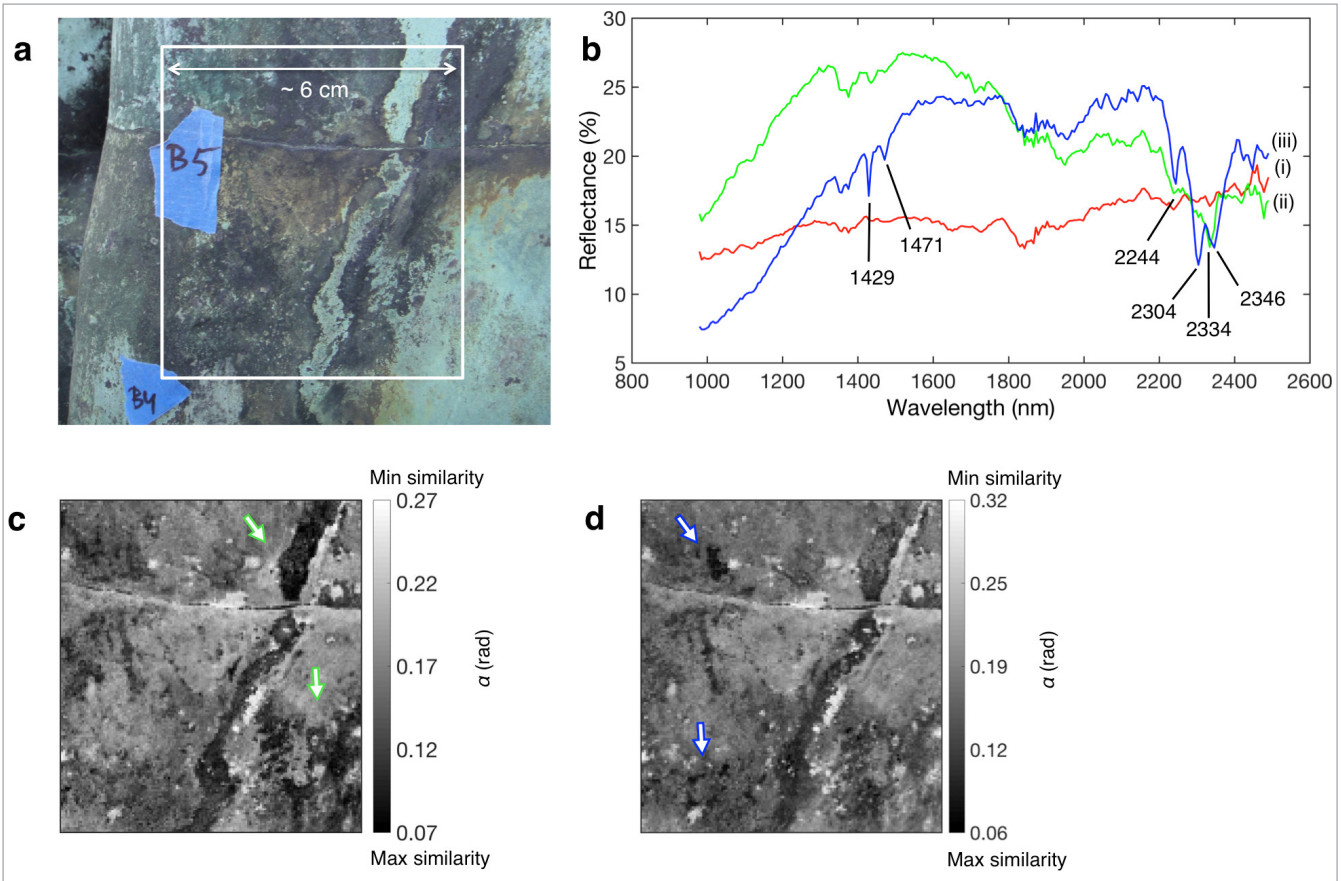

Figure 4. Analysis of the partially sheltered area. (a) RGB image of the investigated area (white rectangle); (b) spectra extracted by IKSFA: (i) unassigned spectrum, (ii) brochantite-assigned spectrum including weak antlerite bands, (iii) antlerite-assigned spectrum; (c) SAM image of brochantite distribution (green arrows point to pixel areas whose spectra have high similarity with the standard spectrum of brochantite); (d) SAM image of antlerite distribution (blue arrows indicate areas whose spectra have high similarity with the standard spectrum of antlerite).

to-noise ratio and no significant spectral features, and can thus not be interpreted. Occurrence of brochantite in exposed areas was confirmed by X-ray diffraction (XRD) of micro-sample collected from the sculpture (Figure SM2 in the Supplementary Material).

Data from the partially sheltered area are shown in Figure 4. In the RGB image (Figure 4a), the investigated area displays several zones of different colours. A pale green colour appears along a strip and in the lower-right corner, while a darkish colour covers the remaining area. SVD indicated the presence of three significant factors. The key set of raw spectra related to the above factors is shown in Figure 4b. As noted before, each spectrum in Figure 4b shows bands in the ranges 1300–1400 nm and 1800–1900 nm due to interference from water vapour. The first spectrum [Figure 4b (i)] is noisy and does not show any characteristic bands that would allow its interpretation. The second spectrum [Figure 4b(ii)] shows the characteristic band of brochantite (νOH + δOH) at 2334 nm as well as two small shoulders at 2304 and 2244 nm, which are characteristic of antlerite. Therefore, the above spectrum indicates that both brochantite and antlerite are present in the analysed area. However, due to the strong band at 2334 nm, it can be assumed that the spectrum is representative of the presence of brochantite. The SAM image of distribution of brochantite is presented in Figure 4c. A comparison with the RGB image (Figure 4a) shows that this compound prevails in the pale green regions of the investigated area, namely, the upper part of the stripe and the lower-right corner (Figure 4c, green arrows). The third spectrum [Figure 4b (iii)] displays the characteristic band-pattern of antlerite with the combination band νOH + δOH at 2304 nm and the first overtone of the νOH at 1429 nm. The SAM image of antlerite distribution (Figure 4d) indicates that this compound is preponderant in certain spots located

in the upper- and lower-left corners in Figure 4d (highlighted by two blue arrows). In this case, the detailed distribution of antlerite cannot be identified by colour in the RGB image. The areas where antlerite is located do not present an identical green colour but appear darkish green or black. Occurrence of both brochantite and antlerite in the partially sheltered area was confirmed by absorption mid-infrared spectroscopy performed on microsamples collected from the area labelled B4 in Figure 4a (Figure SM3 in the Supplementary Material).

This study has shown that SWIR HSI can be used to provide spatial distribution of antlerite and brochantite on a bronze sculpture. Identification of the above compounds was performed by means of overtones and combination bands in the SWIR region. Data analysis and spatial distribution did not involve distinct bands, but whole spectrum profiles. In accordance with the literature,[9–11,13,27] the mechanism of corrosion is not the same all over the sculpture surface as it depends on micro-environmental conditions. Formation of basic copper sulfates is promoted by certain sulfur species in the atmosphere, such as gaseous sulfur dioxide and sulfate ion in aerosols. The primary corrosion product is cuprite (Cu_2O), which within several weeks turns into amorphous copper sulfate. Further, this undergoes slow conversion into langite ($Cu_4SO_4(OH)_6 \bullet 2H_2O$) posnjakite ($Cu_4SO_4(OH)_6 \bullet H_2O$) or strandbergite ($Cu_{2.5}SO_4(OH)_3 \bullet 2H_2O$). Subsequent reactions produce the final corrosion products in a matter of years. In this way, langite and posnjakite turn into brochantite, whereas strandbergite acts as precursor to either antlerite or brochantite depending on the chemical composition of the water film at the surface.[13,17] If only antlerite or brochantite are considered, the formal equilibria between them can be formulated as follows:

$$3Cu_4SO_4(OH)_6 + SO_4^{2-} + 2H^+ \rightleftharpoons 4Cu_3SO_4(OH)_4 + 2H_2O \quad (1)$$

or

$$2Cu_4SO_4(OH)_6 + SO_4^{2-} + Cu^{2+} \rightleftharpoons 3Cu_3SO_4(OH)_4 \quad (2)$$

The above reactions are not kinetically favoured at room temperature,[28] but they provide a thermodynamic rationale for understanding the effect of chemical factors in the formation of the final products. It is obvious that a higher content in sulfate, hydrogen ions and copper ions promotes the formation of antlerite, whereas the opposite conditions favour the formation of brochantite. The main pathway is dictated by local conditions. On sheltered areas, film stagnation allows for slow evaporation leading to enhanced concentrations of ionic species. Therefore, formation of antlerite is favoured. Conversely, on unsheltered areas, the concentrations of sulfate and hydrogen ions cannot overcome those in the precipitation and brochantite formation will prevail. The results in Figure 3 are typical of this situation. However, the results in Figure 4 cannot be ascribed to one of the above limiting situations as the investigated area is only partially sheltered. Consequently, both brochantite and antlerite are found here and, obviously, such intermediate conditions are the most frequent. Figure 4c and 4d demonstrate that centimetre-sized topographical details do favour formation of one or another of the two considered compounds on minute areas.

Conclusion

SWIR HSI proved to be able to determine the spatial distribution of two corrosion products, brochantite and antlerite, on selected areas on a bronze. None of the above compounds can be recognised by visual observation, but HSI data revealed the occurrence of each of them in certain areas. Moreover, non-uniform distribution of the above compounds was clearly evidenced by HSI, but it could escape an investigation of discrete spots.

Being non-destructive and allowing *in situ* analysis of large corroded areas, SWIR HSI can represent an important new tool for the investigation of bronze statuary. To the best of the authors' knowledge, this is the first *in situ* application of SWIR HSI to the assay of atmospheric corrosion of bronze statuary. Further development can be made by exploring the possibility to map other corrosion products that can be detected in this wavelength range. The technique may also find useful application in other corrosion-related fields. Devices that allow the hyperspectral camera to follow the topography of the sculpture can be developed for investigating broader monument areas.

Conflicts of interest

The authors declare no conflict of interest.

Acknowledgements

We thank the Vigeland Museum in the persons of Siri Refsum and Ingebjørg Mogstad for allowing us to perform the investigation of the sculpture at the Museum's courtyard. We are much obliged to Julio Hernandez from NEO (Norsk Elektro Optikk AS) for assistance with collecting the hyperspectral data. We acknowledge financial support from Anders Jahres Fund for Chemistry and Marine Technology and the Environmental and Analytical Chemistry group at NTNU, Department of Chemistry. Dr Florinel-Gabriel Banica and Professor Lise Kvittingen from NTNU, Department of Chemistry, are gratefully acknowledged for useful comments and suggestions.

References

1. M. Kubik, "Hyperspectral imaging: a new technique for the non-invasive study of artworks", in *Physical Techniques in the Study of Art, Archaeology and Cultural Heritage, Vol. 2*, Ed by D.C. Creagh and M.P. Bracciale. Elsevier, Amsterdam, NL, pp. 199–259 (2007).
2. L.L. Randeberg, E.L.P. Larsen and L.O. Svaasand, "Characterization of vascular structures and skin bruises using hyperspectral imaging, image analysis and diffusion theory", *J. Biophotonics* **3,** 53–65 (2010). doi: https://doi.org/10.1002/jbio.200910059
3. B.K. Alsberg and J. Rosvold, "Rapid localization of bone fragments on surfaces using back projection and hyperspectral imaging", *J. Forensic Sci.* **59,** 474–480 (2014). doi: https://doi.org/10.1111/1556-4029.12319
4. A.A. Gowen, C.P. O'Donnell, P.J. Cullen, G. Downey and J.M. Frias, "Hyperspectral imaging–an emerging process analytical tool for food quality and safety control", *Trends Food Sci. Technol.* **18,** 590–598 (2007). doi: https://doi.org/10.1016/j.tifs.2007.06.001
5. J.K. Delaney, J.G. Zeibel, M. Thoury, R. Littleton, M. Palmer, K.M. Morales, E.R. de La Rie and A. Hoenigswald, "Visible and infrared imaging spectroscopy of Picasso's Harlequin musician: mapping and identification of artist materials *in situ*", *Appl. Spectrosc.* **64,** 584–594 (2010). doi: https://doi.org/10.1366/000370210791414443
6. P. Ricciardi, J.K. Delaney, M. Facini, J.G. Zeibel, M. Picollo, S. Lomax and M. Loew, "Near infrared reflectance imaging spectroscopy to map paint binders *in situ* on illuminated manuscripts", *Angew. Chem. Int. Ed.* **51,** 5607–5610 (2012). doi: https://doi.org/10.1002/anie.201200840
7. L. Cséfalvayová, M. Strlič and H. Karjalainen, "Quantitative NIR chemical imaging in heritage science", *Anal. Chem.* **83,** 5101–5106 (2011). doi: https://doi.org/10.1021/ac200986p
8. L.S. Selwyn, N.E. Binnie, J. Poitras, M.E. Laver and D.A. Downham, "Outdoor bronze statues: analysis of metal and surface samples", *Stud. Conserv.* **41,** 205–228 (1996). doi: https://doi.org/10.1179/sic.1996.41.4.205
9. D.A. Scott, *Copper and Bronze in Art: Corrosion, Colorants, Conservation*. The Getty Conservation Institute, Los Angeles, USA (2002).
10. P.D. Weil, P. Gaspar, L. Gulbransen, R. Lindberg and D. Zimmerman, "The corrosive deterioration of outdoor bronze sculpture", *Stud. Conserv.* **27(sup 1),** 130–134 (1982). https://doi.org/10.1179/sic.1982.27.Supplement-1.130
11. D. De la Fuente, J. Simancas and M. Morcillo, "Morphological study of 16-year patinas formed on copper in a wide range of atmospheric exposures", *Corros. Sci.* **50,** 268–285 (2008). doi: https://doi.org/10.1016/j.corsci.2007.05.030
12. C.H. Yoder, T.M. Agee, K.E. Ginion, A.E. Hofmann, J.E. Ewanichak, C.D. Schaeffer Jr, M.J. Carroll, R.W. Schaeffer and P.F. McCaffrey, "The relative stabilities of the copper hydroxyl sulphates", *Mineralogical Magazine* **71,** 571–577 (2007). doi: https://doi.org/10.1180/minmag.2007.071.5.571
13. A. Krätschmer, I. Odnevall Wallinder and C. Leygraf, "The evolution of outdoor copper patina", *Corros. Sci.* **44,** 425–450 (2002). doi: https://doi.org/10.1016/S0010-938X(01)00081-6
14. K.M. Reddy, A.S. Jacob, B.J. Reddy and Y.P. Reddy, "Optical absorption spectra of Cu^{2+} in brochantite", *Phys. Status Solidi B* **139,** K145–K150 (1987). doi: https://doi.org/10.1002/pssb.2221390241
15. R.R.S. Reddy, S.L. Reddy, S.G. Reddy and B.J. Reddy, "Spectral studies of divalent copper in antlerite mineral", *Cryst. Res. Technol.* **37,** 485–490 (2002). doi: https://doi.org/10.1002/1521-4079(200205)37:5<485::AID-CRAT485>3.0.CO;2-E

16. A. Le Normand-Romain, *The Bronzes of Rodin: Catalogue of Works in the Musée Rodin, Vol. 1*. Musée Rodin, Paris (2007).

17. H. Strandberg, "Reactions of copper patina compounds—I. Influence of some air pollutants", *Atmos. Environ.* **32,** 3511–3520 (1998). doi: https://doi.org/10.1016/S1352-2310(98)00057-0

18. A.A. Green, M. Berman, P. Switzer and M.D. Craig, "A transformation for ordering multispectral data in terms of image quality with implications for noise removal", *IEEE Trans. Geosci. Remote Sens.* **26,** 65–74 (1988). doi: https://doi.org/10.1109/36.3001

19. E.R. Malinowski, "Obtaining the key set of typical vectors by factor analysis and subsequent isolation of component spectra", *Anal. Chim. Acta* **134,** 129–137 (1982). doi: https://doi.org/10.1016/S0003-2670(01)84184-2

20. K.J. Schostack and E.R. Malinowski, "Preferred set selection by iterative key set factor analysis", *Chemometr. Intell. Lab.* **6,** 21–29 (1989). doi: https://doi.org/10.1016/0169-7439(89)80062-0

21. F.A. Kruse, A.B. Lefkoff, J.W. Boardman, K.B. Heidebrecht, A.T. Shapiro, P.J. Barloon and A.F.H. Goetz, "The spectral image processing system (SIPS)—interactive visualization and analysis of imaging spectrometer data", *Remote Sens. Environ.* **44,** 145–163 (1993). doi: https://doi.org/10.1016/0034-4257(93)90013-N

22. E. Catelli, L.L. Randeberg, B.K. Alsberg, K.F. Gebremariam and S. Bracci, "An explorative chemometric approach applied to hyperspectral images for the study of illuminated manuscripts", *Spectrochim. Acta A* **177,** 69–78 (2017). doi: https://doi.org/10.1016/j.saa.2017.01.015

23. E.A. Secco, "Spectroscopic properties of SO_4 (and OH) in different molecular and crystalline environments. I. Infrared spectra of $Cu_4(OH)_6SO_4$, $Cu_4(OH)_4OSO_4$, and $Cu_3(OH)_4SO_4$", *Can. J. Chem.* **66,** 329–336 (1988). doi: https://doi.org/10.1139/v88-057

24. R.L. Frost, B.J. Reddy, D.L Wain and W.N. Martens, "Identification of the rosasite group minerals—An application of near infrared spectroscopy", *Spectrochim. Acta A* **66,** 1075–1081 (2007). doi: https://doi.org/10.1016/j.saa.2006.04.043

25. G.R. Hunt, J.W. Salisbury and C.J. Lenhoff, "Visible and infrared spectra of minerals and rocks. IV: Sulphides and sulphates", *Modern Geology* **3,** 1–14 (1971).

26. E. Catelli, G. Sciutto, S. Prati, Y. Jia and R. Mazzeo, "Characterization of outdoor bronze monument patinas: the potentialities of near-infrared spectroscopic analysis", *Environ. Sci. Pollut. Res.* **25,** 24379–24393 (2018). https://doi.org/10.1007/s11356-018-2483-3

27. V. Hayez, J. Guillaume, A. Hubin and H. Terryn, "Micro-Raman spectroscopy for the study of corrosion products on copper alloys: setting up of a reference database and studying works of art", *J. Raman Spectrosc.* **35,** 732–738 (2004). doi: https://doi.org/10.1002/jrs.1194

28. A. Lins and T. Power, "The corrosion of bronze monuments in polluted urban sites: a report on the stability of copper mineral species at different pH levels", in *Ancient and Historic Metals. Conservation and Scientific Research*, Ed by D.A. Schott, J. Podany and B.B. Considine. The J. Paul Getty Trust, Los Angeles, USA, pp. 119–151 (2007).